

Nuclear spin relaxation rate near the disorder-driven quantum critical point in Weyl fermion systems

Tomoki Hirose , Hideaki Maebashi, and Masao Ogata
 Department of Physics, University of Tokyo, Bunkyo, Tokyo 113-0033, Japan

 (Received 27 December 2019; accepted 17 March 2020; published 6 April 2020)

Disorder such as impurities and dislocations in Weyl semimetals drives a quantum critical point (QCP) where the density of states at the Weyl point gains a nonzero value. Near the QCP, the asymptotic low-energy singularities of physical quantities are controlled by the critical exponents ν and z . The nuclear spin-lattice relaxation rate, which originates from the hyperfine coupling between a nuclear spin and long-range orbital currents in Weyl fermion systems, shows intriguing critical behavior. Based on the self-consistent Born approximation for impurities, we study the nuclear spin-lattice relaxation rate $1/T_1$ due to the orbital currents in disordered Weyl SMs. We find that $(T_1 T)^{-1} \sim E^{2/z}$ at the QCP where E is the maximum of temperature T and chemical potential $\mu(T)$ relative to the Weyl point. This scaling behavior of $(T_1 T)^{-1}$ is also confirmed by the self-consistent T -matrix approximation, where a remarkable temperature dependence of $\mu(T)$ could play an important role. We hope these results of $(T_1 T)^{-1}$ will serve as an impetus for exploration of the disorder-driven quantum criticality in Weyl materials.

DOI: [10.1103/PhysRevB.101.155103](https://doi.org/10.1103/PhysRevB.101.155103)

I. INTRODUCTION

In condensed-matter physics, the Weyl Hamiltonian describes an effective model of gapless systems where the inversion or time-reversal symmetry is broken, known as a Weyl semimetal (SM) [1]. Among many candidates, a family of TaAs-type materials is a typical example of Weyl SMs [2–6]. Since the discovery of these materials, the unusual galvanomagnetic transport has attracted much attention. When the electric and magnetic field is applied in parallel, the negative magnetoresistance is predicted due to the chiral anomaly [7,8]. In TaAs-type Weyl SMs, the negative magnetoresistance was experimentally observed [9–12]. Similar studies were carried out on thermoelectric transport. A large positive contribution proportional to the square of the magnetic field was predicted in the longitudinal thermal conductivity when the temperature gradient and magnetic field is applied in parallel [13].

Besides these transport properties, nuclear magnetic resonance (NMR) in Weyl SMs shows unusual dependence of the nuclear spin-lattice relaxation time T_1 on temperature T . In general, the inverse of $T_1 T$ detects local fluctuations of a magnetic field produced at a nuclear spin site by the surrounding electrons [14]. It is usually scaled as the square of the density of states, called the Korringa relation [15,16]. Since the density of states in Weyl SMs is proportional to the square of the energy around the Weyl point, a naive power counting based on the Korringa relation expects that $(T_1 T)^{-1} \sim \max[\mu(T)^4, T^4]$, where $\mu(T)$ is the chemical potential measured from the Weyl point. However, recent nuclear quadrupole resonance (NQR) experiments on TaP revealed that $(T_1 T)^{-1} \sim \max[\mu(T)^2, T^2]$ in Weyl SMs with remarkable temperature dependence of $\mu(T)$ [17,18]. This unusual scaling had been predicted as an orbital effect in $(T_1 T)^{-1}$

which originates from the hyperfine coupling between a nuclear spin and long-range orbital currents of Weyl fermions [19,20]. The importance of the temperature dependence of $\mu(T)$ in gapless systems was also pointed out in relation to the Hall coefficient observed in α -(BEDT-TTF)₂I₃ [21–23].

In the past, orbital magnetism has been studied extensively in Dirac materials, which are narrow-gap electron systems described by the Dirac Hamiltonian [24,25]. The large diamagnetism of bismuth-antimony alloys Bi_{1-x}Sb_x demonstrated a significant contribution from the interband matrix element of the current operator [26,27]. Recently, it was shown to be a counterpart of the inverse of the charge renormalization factor in quantum electrodynamics [28]. Furthermore, $(T_1 T)^{-1}$ in Dirac electron systems was found to be proportional to T^2 due to the orbital effect when temperature is higher than the band gap [20]. This finding partly explains the temperature dependence of $1/T_1$ observed in the β -detected NMR experiment on Bi_{0.9}Sb_{0.1} [29].

Following the work by Lee and Nagaosa, we consider the relaxation of nuclear spins due to local fluctuations of the Biot-Savart magnetic field produced by the orbital current [30]. This is equivalent with the relaxation of nuclear spins from the orbital hyperfine coupling [19,31]. Since the fluctuation of currents is related to the conductivity, this approach allows us to use the field theoretical method for disordered systems. The nuclear spin-lattice relaxation is written in terms of the transverse conductivity $\sigma_T(q, \omega)$ with a wave vector q and frequency ω as

$$\frac{1}{T_1 T} = \frac{4k_B}{3} \gamma_n^2 \mu_0^2 \int \frac{d^3 q}{(2\pi)^3} \frac{1}{q^2} \text{Re} \sigma_T(q, \omega_0), \quad (1)$$

where γ_n , μ_0 , and ω_0 are the gyromagnetic ratio of a nucleus, the vacuum permeability, and the nuclear Larmor frequency,

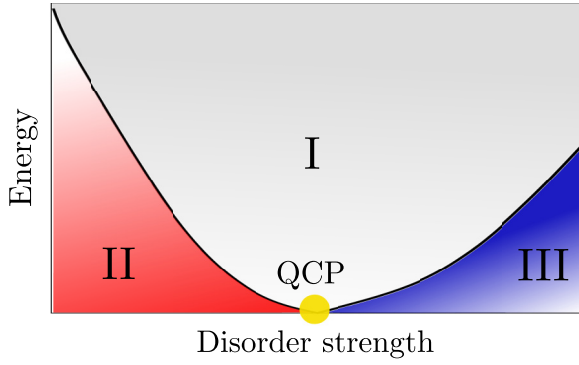


FIG. 1. Schematic energy-disorder phase diagram for disordered Weyl SMs.

respectively. For Dirac electron systems with an electronic charge $-e$, effective mass m^* , and half band gap Δ , Eq. (1) leads to [32]

$$\frac{1}{T_1 T} = \frac{2\pi k_B}{3} \gamma_n^2 \mu_0^2 e^2 c^{*4} \hbar^3 \times \int_{-\infty}^{\infty} dE \left[-\frac{\partial n_F(E)}{\partial E} \right] \frac{D^2(E)}{E^2} \ln \frac{2(E^2 - \Delta^2)}{|E|\omega_0}, \quad (2)$$

where $n_F(E) = [e^{(E-\mu)/k_B T} + 1]^{-1}$ is the Fermi distribution function and $D(E)$ is the density of states. In the low-electron density limit of $\mu \rightarrow \Delta$ with $\mu > \Delta$, Eq. (2) corresponds to the result for free electron gas [33], which shows the usual scaling $(T_1 T)^{-1} \sim D^2(\mu) \sim \mu - \Delta$ (except the logarithmic dependence). On the other hand, Eq. (2) provides the result for Weyl SMs in the gapless limit of $\Delta \rightarrow 0$ with fixing $c^* \equiv \sqrt{\Delta/m^*}$, which shows the unusual scaling $(T_1 T)^{-1} \sim E^2$ with E the maximum of T and μ [19]. We thus see that the origin of the unusual scaling is attributed to the gapless structure of the density of states. It is, however, known that the density of states in gapless systems is sensitive to the presence of disorder such as impurities and dislocations. Then a natural question arises: *How does the scaling behavior of $(T_1 T)^{-1}$ change by introducing the disorder?*

The disorder-induced quantum critical point (QCP) exists in d -dimensional gapless systems with a dispersion $E_k \propto k^\alpha$ under the short-ranged disorder [34–37]. When $d < 2\alpha$, the gapless structure of the density of states disappears by infinitesimal disorder. When $d > 2\alpha$, on the other hand, it is robust against weak disorder below the critical strength, leading to the disorder-driven QCP. Since $d = 3$ and $\alpha = 1$ for Weyl SMs, disordered Weyl SMs have the QCP [38–55]. Here, we should note that the critical behavior is correct only up to rare-event effects [39,40]. In Fig. 1, we present a schematic energy-disorder phase diagram, showing three different regimes distinguished by the energy dependence of the density of states. In regime I, the energy dependence of the density of states are dominated by the QCP. Regime II corresponds to weakly disordered systems at low energy, where the power law is qualitatively equivalent with clean systems. In regime III, the density of states becomes nonzero at the Weyl point. The frequency and temperature dependencies of the optical conductivity in these regimes were theoretically predicted in addition to the thermodynamic properties [52,53].

In this paper, we study the nuclear spin-lattice relaxation rate due to orbital currents in disordered Weyl SMs using the self-consistent Born approximation (SCBA) for impurities. For the critical exponents $z = 2$ and $\nu = 1$ within the SCBA, we find that our result is in agreement with the scaling relation of $(T_1 T)^{-1}$. At $E_F = 0$, the nuclear spin-lattice relaxation rate is scaled as $(T_1 T)^{-1} \sim T^{2/z}$, $(T_1 T)^{-1} \sim T^2$, and $(T_1 T)^{-1} \sim (W - W_c)^{2\nu}$ in the regimes I, II, and III, respectively, where we denote the disorder strength as W and its critical value as W_c . We also discuss the relationship to the one-loop renormalization group (RG) analysis, which gives $z = 1.5$ [49]. When the Weyl points are away from the Fermi energy, deviations from these behaviors are elucidated with a special emphasis on the temperature dependence of $\mu(T)$. In particular, we show that a remarkable temperature dependence of $\mu(T)$ caused by impurities amplifies an additional feature of $(T_1 T)^{-1}$ with a low-temperature upturn in the regime II, which is consistent with the recent NQR experiment on TaP [17,18].

The organization of this paper is as follows. In Sec. II, we introduce the SCBA for a pair of Weyl nodes with the opposite chirality. In Sec. III, the impurity-averaged transverse conductivity is derived as a function of a wave vector q . To derive the vertex correction in a gauge-invariant manner, we employ the conserving approximation for the SCBA. We find that the vertex correction leads to quantitative changes in $(T_1 T)^{-1}$ but does not affect the critical behavior. In Sec. IV, the nuclear spin-lattice relaxation rate is computed numerically. We also predict the scaling relation of $(T_1 T)^{-1}$ from the dimensional analysis, which is in agreement with the SCBA. In Secs. V and VI, we discuss the effect of the particle-hole asymmetry within the self-consistent T -matrix approximation (SCTA) and its implication in experiments. In the final section, we provide a summary of this paper.

II. MODEL HAMILTONIAN AND THE DISORDER-DRIVEN QUANTUM CRITICALITY

A. Model

We consider a pair of Weyl nodes with the opposite chirality. For $2N$ nodes, we simply need to multiply our result by a factor of N . With random disorder potential, the Hamiltonian $H = H_0 + H_D$ is given as follows:

$$H_0 = \sum_{a=\mathcal{L},\mathcal{R}} \int dk \psi_{k,a}^\dagger \chi_a \hbar c^* \mathbf{k} \cdot \boldsymbol{\sigma} \psi_{k,a}, \quad (3)$$

$$H_D = \sum_{a,b=\mathcal{L},\mathcal{R}} \int dk \psi_{k,a}^\dagger u_{ab} \psi_{k,b}, \quad (4)$$

where c^* is the Fermi velocity, σ_i are the Pauli matrices, and \mathcal{L}/\mathcal{R} stands for left/right chiral modes with $\chi_{\mathcal{L}/\mathcal{R}} = \pm 1$. The intravalley scattering is assumed to be isotropic ($|u_{\mathcal{L}\mathcal{L}}|^2 = |u_{\mathcal{R}\mathcal{R}}|^2$). In addition, the intervalley scattering $u_{\mathcal{L}\mathcal{R}} = u_{\mathcal{R}\mathcal{L}}^*$ is introduced. We should note that a similar model was discussed in graphene [56–60].

If the range of the impurity potential is much shorter than the lattice constant, the intervalley scattering becomes important. In contrast, it is suppressed for the potential with its range comparable to the lattice constant. Following Ref. [56], we consider the short-range scatters ($|u_{\mathcal{L}\mathcal{R}}|^2 = |u_{\mathcal{L}\mathcal{L}}|^2$) and

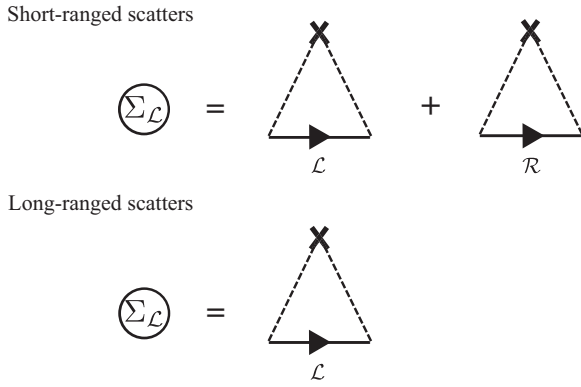


FIG. 2. Feynman diagram for the self-energy of a Weyl point with left chirality with the short-range scatters ($|u_{\mathcal{L}\mathcal{R}}|^2 = |u_{\mathcal{L}\mathcal{L}}|^2$) and the long-range scatters ($|u_{\mathcal{L}\mathcal{R}}|^2 = 0$). The subscript \mathcal{L}/\mathcal{R} implies the chirality.

the long-range scatters ($|u_{\mathcal{L}\mathcal{R}}|^2 = 0$). In both limiting cases, we assume that the range of the impurity potential is much smaller than the typical electron wavelength.

In the SCBA, the self-energy is obtained by solving the following self-consistent equation (Fig. 2):

$$\Sigma_a^{\mathcal{R}}(\omega) = \frac{n_i}{\hbar^2} \sum_{\mathbf{k}} \sum_{b=\mathcal{L},\mathcal{R}} |u_{ab}|^2 G_b^{\mathcal{R}}(\mathbf{k}, \omega), \quad (5)$$

where the subscript a denotes the chirality \mathcal{L}/\mathcal{R} , n_i is the impurity concentration, and $G_a^{\mathcal{R}}$ is the retarded Green's function after disorder averaging. The disorder-averaged Green's function is defined as

$$G_a^{\mathcal{R}}(\mathbf{k}, \omega) = [\omega + \mu/\hbar - \chi_a c^* \boldsymbol{\sigma} \cdot \mathbf{k} - \Sigma_a^{\mathcal{R}}(\omega)]^{-1}. \quad (6)$$

We should note that the self-energy takes the same form for both short-ranged and long-ranged scatters. Assuming $\Sigma^{\mathcal{R}}(\omega) = \Sigma_1^{\mathcal{R}}(\omega)\sigma_0$ with σ_0 denoting the identity matrix element, the self-consistent equation is simplified to

$$\begin{aligned} \Sigma_1^{\mathcal{R}}(\omega) &= \frac{n_i(|u_{\mathcal{L}\mathcal{L}}|^2 + |u_{\mathcal{R}\mathcal{L}}|^2)}{\hbar^2} \int \frac{dk^3}{(2\pi)^3} \left[\frac{\tilde{\omega}_{\mathcal{R}}}{(\tilde{\omega}_{\mathcal{R}})^2 - c^*2k^2} \right] \\ &= W\tilde{\omega}_{\mathcal{R}}f(\omega), \end{aligned} \quad (7)$$

where $\tilde{\omega}_{\mathcal{R}} = \omega + \mu/\hbar - \Sigma_1^{\mathcal{R}}(\omega)$. Since the momentum integration in the above equation is divergent, we introduce the cutoff factor $\frac{k_c^2}{k_c^2 + k^2}$ to take account of the finite band width. The dimensionless impurity strength W and the function $f(\omega)$ are defined as follows:

$$W = \frac{n_i E_c}{2\pi^2 \hbar^3 c^*3} (|u_{\mathcal{L}\mathcal{L}}|^2 + |u_{\mathcal{R}\mathcal{L}}|^2), \quad (8)$$

$$f(\omega) = \int_0^\infty \frac{K^2 dK}{K^2 + 1} \frac{1}{\tilde{\Omega}_{\mathcal{R}}^2 - K^2} = -\frac{\pi}{2} \frac{1}{1 - i\tilde{\Omega}_{\mathcal{R}}}, \quad (9)$$

where the energy cutoff is $E_c = \hbar c^* k_c$ and the dimensionless quantities are $\tilde{\Omega}_{\mathcal{R}} = \hbar\tilde{\omega}_{\mathcal{R}}/E_c$ and $K = \hbar c^* k/E_c$. The self-consistent solution is obtained as

$$\tilde{\Omega}_{\mathcal{R}} = \frac{1}{2}(i\delta + \Omega + \text{sgn}(\Omega)\sqrt{4i\Omega + (i\delta + \Omega)^2}), \quad (10)$$

with $\delta = W/W_c - 1$, $W_c = 2/\pi$ is the critical impurity strength, and $\Omega = (\hbar\omega + \mu)/E_c$. The density of states

$D(\omega)$ is

$$\begin{aligned} D(\omega) &= -\frac{1}{\hbar\pi} \sum_{a=\mathcal{L},\mathcal{R}} \sum_{\mathbf{k}} \text{Im tr}[G_a^{\mathcal{R}}(\mathbf{k}, \omega)] \\ &= -\frac{2E_c^2}{(\pi\hbar c^*)^3} \text{Im}[\tilde{\Omega}_{\mathcal{R}} f(\omega)]. \end{aligned} \quad (11)$$

At $\Omega = 0$, we have a simple criterion for the criticality as $\tilde{\Omega}_{\mathcal{R}} = i\delta$ for $\delta > 0$ and $\tilde{\Omega}_{\mathcal{R}} = 0$ otherwise.

B. Critical exponents in the SCBA

The disorder-induced quantum criticality is characterized by universal critical exponents. Near the QCP in disordered Weyl SMs, the density of states acts as the order parameter that is described by the critical exponents z and ν . The dynamical exponent z relates the correlation length ξ and the characteristic energy scale Ω_0 as $\Omega_0 \sim \xi^{-z}$. At the QCP, the correlation length diverges as $\xi \sim \delta^{-\nu}$.

From the scaling of the density of states, the density of states at the QCP is [37,38,55]

$$D(\Omega, \delta = 0) \sim \Omega^{\frac{d}{z}-1}, \quad (12)$$

where d is the spatial dimension of the system. Above the QCP, the density of states becomes finite even at Weyl nodes. At $\Omega = 0$, it is given as

$$D(\Omega = 0, \delta > 0) \sim \delta^{(d-z)\nu}. \quad (13)$$

Below the criticality, the density of states for $\Omega \ll 1$ has the same energy dependence as Weyl SMs without disorder.

The solution of Eq. (5) matches with the result of the saddle-point solution in the limit of $N \rightarrow \infty$ valleys. Thus, the critical exponents in the SCBA are given by $z = 2$ and $\nu = 1$ [61]. At the QCP ($\delta = 0$), $\tilde{\Omega}^{\mathcal{R}} \sim (1+i)\sqrt{\frac{\Omega}{2}}$ for $\Omega \rightarrow 0$. The density of states for small Ω is

$$D(\Omega) \approx \frac{E_c^2}{\pi^2(\hbar c^*)^3} \sqrt{\frac{\Omega}{2}}, \quad (14)$$

leading to $z = 2$. In Fig. 3(a), the density of states against Fermi energy E_F is plotted near the critical point $W = W_c$. At the critical point, the gradient of density of states at Weyl points is divergent, showing the root-squared energy dependence. Similarly, the density of states at $\Omega = 0$ for $\delta > 0$ is given by

$$D(\delta) \approx \frac{E_c^2}{\pi^2(\hbar c^*)^3} \delta. \quad (15)$$

Hence, $\nu = 1$.

C. Chemical potential at finite temperatures

Since the nuclear spin-lattice relaxation rate $1/T_1$ is measured against temperatures, the temperature dependence of chemical potential is important. In this section, we consider the effect of impurity on the chemical potential at finite temperatures. Assuming that a total number of charge carriers is conserved in two bands forming a Weyl cone, we obtain the

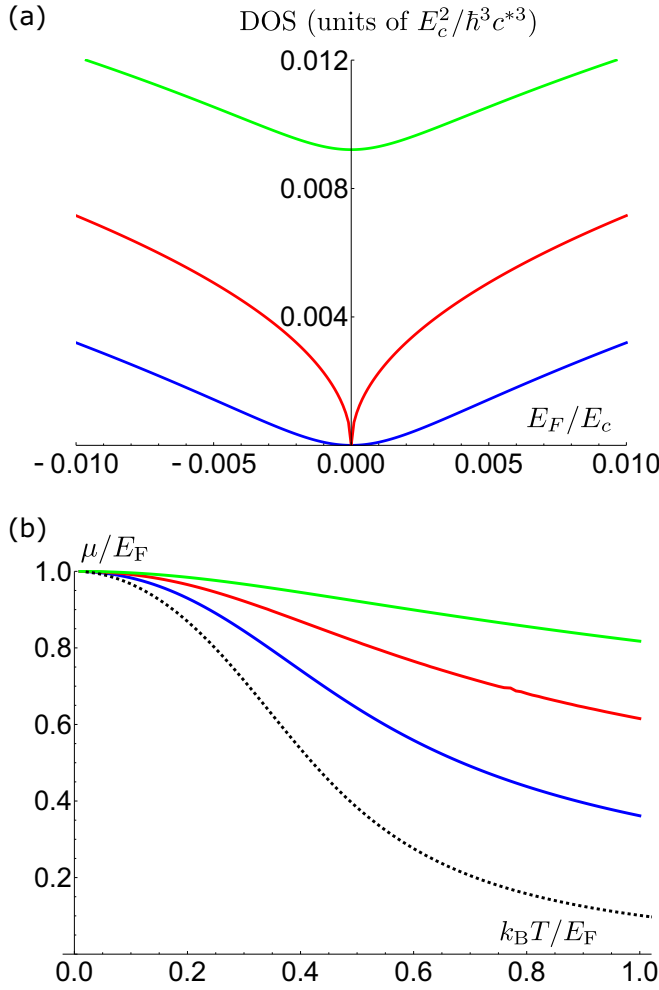


FIG. 3. (a) The density of states in the SCBA against Fermi energy $E_F = \mu(T = 0)$. (b) Chemical potential against temperatures for $E_F/E_c = 10^{-2}$. A dashed line corresponds to the clean system. The impurity strength for both plots are set at $W/W_c = 0.9$ (blue), 1.0 (red), and 1.1 (green) from the bottom.

temperature-dependent chemical potential $\mu(T)$. The particle and hole numbers are given as

$$n = \int_0^\infty dE n_F(E) D(E), \quad (16)$$

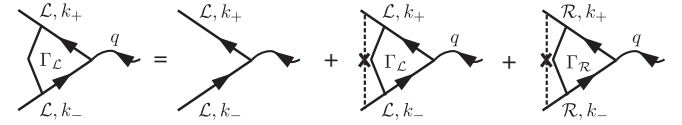
$$p = \int_{-\infty}^0 dE (1 - n_F(E)) D(E). \quad (17)$$

The change in the total carrier number from $T = 0$ to $T = T'$ is given by

$$\begin{aligned} \delta N &= (n - p)|_{T=T'} - (n - p)|_{T=0} \\ &= \int_{-\infty}^\infty dE n_F(E) D(E) - \int_{-\infty}^{E_F} dE D(E), \end{aligned} \quad (18)$$

where $E_F = \mu(T = 0)$ is the Fermi energy. In our calculation, chemical potential is numerically computed by keeping $\delta N = 0$ with the renormalized density of states under impurity. The integration over energy is taken for a finite width scaled by temperatures, neglecting a small contribution from high-energy regions.

Short-ranged scatters



Long-ranged scatters

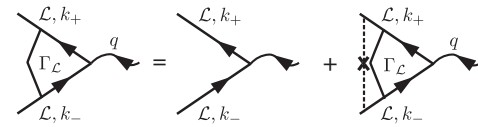


FIG. 4. Feynman diagram for the vertex function of a left chiral mode with the short-range scatters ($|u_{\mathcal{L}\mathcal{R}}|^2 = |u_{\mathcal{L}\mathcal{L}}|^2$) and the long-range scatters ($|u_{\mathcal{L}\mathcal{R}}|^2 = 0$). The subscript \mathcal{L}/\mathcal{R} implies the chirality.

In Fig. 3(b), chemical potential is plotted against temperatures near the critical point. In the SCBA, the density of states is symmetric about Weyl nodes. As a result, chemical potential moves toward Weyl points as the temperature increases. For weak disorder strength, the temperature dependence is almost identical with the clean system, showing a large decrease below $k_B T/E_F \sim 1$. As the impurity strength approaches the critical value, the change in chemical potential becomes smaller.

III. TRANSVERSE CONDUCTIVITY

A. Formulation

In this section, we obtain the static conductivity tensor $\sigma_{ij}(\mathbf{q})$ for the disordered Weyl fermion systems, whose transverse part will be used for computation of $1/T_1$ in the next section. By applying the standard Feynman diagrammatic technique based on the Kubo formula to our systems, the conductivity tensor is given by

$$\begin{aligned} \sigma_{ij}(\mathbf{q}) &= \frac{e^2 c^{*2}}{\hbar} \text{Re} \sum_{|\mathbf{k}| < k_c} \sum_{a=\mathcal{L}, \mathcal{R}} \int_{-\infty}^\infty \frac{d\omega}{2\pi} \left(-\frac{\partial n_F(\omega)}{\partial \omega} \right) \\ &\quad \times \text{Tr} \left[\sigma_i G_a^R(\mathbf{k}_-, \omega) \Gamma_{a,j}^{\text{RA}}(\omega; \mathbf{q}) G_a^A(\mathbf{k}_+, \omega) \right. \\ &\quad \left. - \sigma_i G_a^R(\mathbf{k}_-, \omega) \Gamma_{a,j}^{\text{RR}}(\omega; \mathbf{q}) G_a^R(\mathbf{k}_+, \omega) \right], \end{aligned} \quad (19)$$

where $\mathbf{k}_\pm = \mathbf{k} \pm \mathbf{q}/2$. Here the current vertex function is defined as $\chi_a c^* \Gamma_{a,j}^{\alpha\beta}(\omega; \mathbf{q})$ with $a = \mathcal{L}/\mathcal{R}$, where the superscript α, β stands for R/A in relation to the retarded/advanced Green's functions. As in the previous section, we take a smooth cutoff procedure for a wave-number cutoff k_c as

$$\sum_{|\mathbf{k}| < k_c} \longrightarrow \int \frac{d^3 k}{(2\pi)^3} \frac{k_c^2}{|\mathbf{k}|^2 + k_c^2}. \quad (20)$$

1. Conserving approximation

To preserve gauge invariance, we introduce a conserving approximation corresponding to the SCBA with special care about the wave-number cutoff k_c of the \mathbf{k} summation. The Bethe-Salpeter equation for the vertex function $\Gamma_{a,j}^{\alpha\beta}(\omega; \mathbf{q})$ is

then given by (Fig. 4)

$$\Gamma_{a,j}^{\alpha\beta}(\omega; \mathbf{q}) = \sigma_j + \frac{n_i}{\hbar^2} \sum_{|\mathbf{k}| < k_c} \sum_{b=\mathcal{L}, \mathcal{R}} \chi_a |u_{ab}|^2 \chi_b \times G_b^\alpha(\mathbf{k}_-, \omega) \Gamma_{b,j}^{\alpha\beta}(\omega; \mathbf{q}) G_b^\beta(\mathbf{k}_+, \omega). \quad (21)$$

Here the Green's functions $G_a^\alpha(\mathbf{k}_\pm, \omega)$ in Eqs. (19) and (21) are redefined so as to incorporate an effect of the wave-number cutoff k_c as

$$G_a^\alpha(\mathbf{k}_\pm, \omega) = [\omega + \mu/\hbar - \chi_a c^* \boldsymbol{\sigma} \cdot \mathbf{k}_\pm - \Sigma_a^\alpha(\omega; \pm \mathbf{q}/2)]^{-1}, \quad (22)$$

where the self-consistent equation for the self-energy correction $\Sigma_a^\alpha(\omega; \pm \mathbf{q}/2)$ is given by

$$\Sigma_a^\alpha(\omega; \pm \mathbf{q}/2) = \frac{n_i}{\hbar^2} \sum_{|\mathbf{k}| < k_c} \sum_{b=\mathcal{L}, \mathcal{R}} |u_{ab}|^2 G_b^\alpha(\mathbf{k}_\pm, \omega). \quad (23)$$

It is, here, emphasized that the self-consistent equation for $\Sigma_a^\alpha(\omega)$ in Sec. II is modified as Eq. (23), so the self-energy correction $\Sigma_a^\alpha(\omega; \pm \mathbf{q}/2)$ in the conductivity tensor becomes dependent on \mathbf{q} . This modification of the self-consistent equation is necessary to preserve gauge invariance for the theory with a finite cutoff k_c .

Now we consider the Bethe-Salpeter equation given by Eq. (21). Because any 2×2 matrix can be written as a linear combination of the Pauli matrices σ_i and the identity matrix $\sigma_0 = I_{2 \times 2}$, the vertex function $\Gamma_{a,j}^{\alpha\beta}(\omega; \mathbf{q})$ is expanded as $\Gamma_{a,j}^{\alpha\beta}(\omega; \mathbf{q}) = \sum_{\nu=0}^3 \sigma_\nu \Gamma_{a,\nu j}^{\alpha\beta}(\omega; \mathbf{q})$, where the expansion coefficient is given by

$$\Gamma_{a,\nu j}^{\alpha\beta}(\omega; \mathbf{q}) = \frac{1}{2} \text{Tr}[\sigma_\nu \Gamma_{a,j}^{\alpha\beta}(\omega; \mathbf{q})]. \quad (24)$$

Then we can write Eq. (21) as

$$\Gamma_{a,\mu j}^{\alpha\beta}(\omega; \mathbf{q}) = \delta_{\mu j} + \frac{n_i E_c}{2\pi^2 \hbar^3 c^{*3}} \sum_{b=\mathcal{L}, \mathcal{R}} |u_{ab}|^2 \times \sum_{\nu=0}^3 \Xi_{b,\mu\nu}^{\alpha\beta}(\omega; \mathbf{q}) \Gamma_{b,\nu j}^{\alpha\beta}(\omega; \mathbf{q}), \quad (25)$$

where the dimensionless function $\Xi_{a,\mu\nu}^{\alpha\beta}(\omega; \mathbf{q})$ that includes only the self-energy corrections is defined as

$$\Xi_{a,\mu\nu}^{\alpha\beta}(\omega; \mathbf{q}) = \frac{\pi^2 \hbar c^{*3}}{E_c} \sum_{|\mathbf{k}| < k_c} \text{Tr}[\sigma_\mu G_a^\alpha(\mathbf{k}_-, \omega) \sigma_\nu G_a^\beta(\mathbf{k}_+, \omega)]. \quad (26)$$

In the following, we give explicit expressions for the self-energy corrections and the vertex functions to obtain the wave-number-dependent conductivity.

2. Self-energy corrections

To obtain the function $\Xi_{a,\mu\nu}^{\alpha\beta}(\omega; \mathbf{q})$, we assume that the solution of Eq. (23) is given by

$$\Sigma_a^\alpha(\omega; \pm \mathbf{q}/2) = \Sigma_I^\alpha(\omega; q/2) \sigma_0 \pm \frac{\chi_a c^* \mathbf{q} \cdot \boldsymbol{\sigma}}{2} \times [Z_L^\alpha(\omega; q/2) - 1]. \quad (27)$$

Then we can write the Green's function, Eq. (22), as

$$G_a^\alpha(\mathbf{k}_\pm, \omega) = [\tilde{\omega}_\alpha - \chi_a c^* \boldsymbol{\sigma} \cdot (\mathbf{k} \pm \tilde{\mathbf{q}}_\alpha/2)]^{-1}, \quad (28)$$

where $\tilde{\omega}_\alpha = \omega + \mu/\hbar - \Sigma_I^\alpha(\omega; q/2)$ and $\tilde{\mathbf{q}}_\alpha = Z_L^\alpha(\omega; q/2) \mathbf{q}$.

Substituting Eq. (28) into Eq. (26), we find $\Xi_{a,\mu\nu}^{\alpha\beta}(\omega; \mathbf{q})$ has the form as

$$\Xi_{a,i0}^{\alpha\beta}(\omega; \mathbf{q}) = \Xi_{a,0i}^{\alpha\beta}(\omega; \mathbf{q}) = \chi_a \frac{q_i}{q} \tilde{\Xi}_L^{\alpha\beta}(\omega; q), \quad (29)$$

$$\Xi_{a,ij}^{\alpha\beta}(\omega; \mathbf{q}) = \frac{q_i q_j}{q^2} \Xi_L^{\alpha\beta}(\omega; q) + \left(\delta_{ij} - \frac{q_i q_j}{q^2} \right) \Xi_T^{\alpha\beta}(\omega; q) + i \chi_a \epsilon_{ijk} \frac{q_k}{q} \tilde{\Xi}_T^{\alpha\beta}(\omega; q), \quad (30)$$

where ϵ_{ijk} is the Levi-Civita tensor and the expressions for $\tilde{\Xi}_{L/T}^{\alpha\beta}$, $\Xi_{L/T}^{\alpha\beta}$ are given in Appendix A.

3. Vertex functions

Here, we obtain the expressions for vertex functions, which do not vanish for $q > 0$ in general. The solution of Eq. (25) can be obtained in the same form as Eqs. (29) and (30) to find

$$\Gamma_{a,i0}^{\alpha\beta}(\omega; \mathbf{q}) = \Gamma_{a,0i}^{\alpha\beta}(\omega; \mathbf{q}) = \chi_a \frac{q_i}{q} \tilde{\Gamma}_L^{\alpha\beta}(\omega; q), \quad (31)$$

$$\Gamma_{a,ij}^{\alpha\beta}(\omega; \mathbf{q}) = \frac{q_i q_j}{q^2} \Gamma_L^{\alpha\beta}(\omega; q) + \left(\delta_{ij} - \frac{q_i q_j}{q^2} \right) \Gamma_T^{\alpha\beta}(\omega; q) + i \chi_a \epsilon_{ijk} \frac{q_k}{q} \tilde{\Gamma}_T^{\alpha\beta}(\omega; q). \quad (32)$$

By virtue of the Ward identity, the longitudinal vertex functions $\Gamma_L^{\alpha\beta}(\omega; q)$ and $\tilde{\Gamma}_L^{\alpha\beta}(\omega; q)$ are directly related to the self-energy correction, Eq. (27), as

$$\Gamma_L^{\text{RR}}(\omega; q) = Z_L^{\text{R}}(\omega; q/2), \quad (33)$$

$$\tilde{\Gamma}_L^{\text{RR}}(\omega; q) = 0, \quad (34)$$

$$\Gamma_L^{\text{RA}}(\omega; q) = \text{Re} Z_L^{\text{R}}(\omega; q/2), \quad (35)$$

$$\tilde{\Gamma}_L^{\text{RA}}(\omega; q) = -\frac{2i}{c^* q} \text{Im} \Sigma_I^{\text{R}}(\omega; q/2). \quad (36)$$

On the other hand, the transverse vertex functions $\Gamma_T^{\alpha\beta}(\omega; q)$ and $\tilde{\Gamma}_T^{\alpha\beta}(\omega; q)$ cannot be determined from the Ward identity. They are given in terms of $\Xi_T^{\alpha\beta}(\omega; q)$ and $\tilde{\Xi}_T^{\alpha\beta}(\omega; q)$ as

$$\Gamma_T^{\alpha\beta}(\omega; q) = [1 - W \Xi_T^{\alpha\beta}(\omega; q)] / [[1 - W \Xi_T^{\alpha\beta}(\omega; q)] \times [1 - W_- \Xi_T^{\alpha\beta}(\omega; q)] - W W_- \tilde{\Xi}_T^{\alpha\beta}(\omega; q)^2], \quad (37)$$

$$\tilde{\Gamma}_T^{\alpha\beta}(\omega; q) = W \tilde{\Xi}_T^{\alpha\beta}(\omega; q) / [[1 - W \Xi_T^{\alpha\beta}(\omega; q)] \times [1 - W_- \Xi_T^{\alpha\beta}(\omega; q)] - W W_- \tilde{\Xi}_T^{\alpha\beta}(\omega; q)^2], \quad (38)$$

where W_- is given by

$$W_- = \frac{n_i E_c}{2\pi^2 \hbar^3 c^{*3}} (|u_{\mathcal{L}\mathcal{L}}|^2 - |u_{\mathcal{L}\mathcal{R}}|^2). \quad (39)$$

4. Wave-number-dependent conductivity

By using Eqs. (24) and (26), we write the conductivity tensor, Eq. (19), as

$$\begin{aligned} \sigma_{ij}(\mathbf{q}) &= \frac{e^2 E_c}{2\pi^3 \hbar^2 c^*} \int_{-\infty}^{\infty} d\omega \left(-\frac{\partial n_F(\omega)}{\partial \omega} \right) \\ &\times \sum_{a=\mathcal{L}, \mathcal{R}} \sum_{\mu=0}^3 \text{Re} \left[\Xi_{a,i\mu}^{\text{RA}}(\omega; \mathbf{q}) \Gamma_{a,\mu j}^{\text{RA}}(\omega; \mathbf{q}) \right. \\ &\quad \left. - \Xi_{a,i\mu}^{\text{RR}}(\omega; \mathbf{q}) \Gamma_{a,\mu j}^{\text{RR}}(\omega; \mathbf{q}) d \right], \end{aligned} \quad (40)$$

Substituting Eqs. (29)–(32) into this equation, we find the conductivity tensor has the form

$$\sigma_{ij}(\mathbf{q}) = \frac{q_i q_j}{q^2} \sigma_L(q) + \left(\delta_{ij} - \frac{q_i q_j}{q^2} \right) \sigma_T(q). \quad (41)$$

It is to be noted that the term including ϵ_{ijk} similar to the third terms in Eqs. (30) and (32) vanishes by taking the summation with respect to the chirality $a = \mathcal{L}/\mathcal{R}$. Then we obtain the transverse conductivity $\sigma_T(q)$ as

$$\begin{aligned} \sigma_T(q) &= \sigma_{\text{unit}} \int_{-\infty}^{\infty} d\omega \left(-\frac{\partial n_F(\omega)}{\partial \omega} \right) \text{Re} \left[\Xi_{\text{T}}^{\text{RA}}(\omega; q) \Gamma_{\text{T}}^{\text{RA}}(\omega; q) \right. \\ &\quad \left. - \Xi_{\text{T}}^{\text{RR}}(\omega; q) \Gamma_{\text{T}}^{\text{RR}}(\omega; q) + \tilde{\Xi}_{\text{T}}^{\text{RA}}(\omega; q) \tilde{\Gamma}_{\text{T}}^{\text{RA}}(\omega; q) \right. \\ &\quad \left. - \tilde{\Xi}_{\text{T}}^{\text{RR}}(\omega; q) \tilde{\Gamma}_{\text{T}}^{\text{RR}}(\omega; q) \right], \end{aligned} \quad (42)$$

and the longitudinal conductivity $\sigma_L(q)$ by replacing the subscript T by L in Eq. (42). Here σ_{unit} has the dimension of conductivity as

$$\sigma_{\text{unit}} = \frac{e^2 E_c}{\pi^3 \hbar^2 c^*}. \quad (43)$$

B. Results

As derived in Appendix B, an approximate solution of Eq. (23) for $q/k_c \ll 1$ are given by Eq. (27) with

$$\tilde{\Omega}_{\text{R}}(\omega) = \frac{1}{2} (i\delta + \Omega + \text{sgn}(\Omega) \sqrt{4i\Omega + (i\delta + \Omega)^2}), \quad (44)$$

$$Z_{\text{L}}^{\text{R}}(\omega) = 1 - \frac{W_- \pi (i + 2\tilde{\Omega}_{\text{R}}(\omega))}{\pi W_- [i + 2\tilde{\Omega}_{\text{R}}(\omega)] - 12i [i + \tilde{\Omega}_{\text{R}}(\omega)]^2}, \quad (45)$$

where $\delta = W/W_c - 1$, $\tilde{\Omega}_{\text{R}} = \hbar \tilde{\omega}_{\text{R}}/E_c$ and $\Omega = (\hbar \omega + \mu)/E_c$. Since we are interested in the q dependence of the transverse conductivity $\sigma_T(q)$ for $q/k_c \ll 1$, we take Eqs. (44) and (45) as the self-energy corrections. Here, $\tilde{\omega}_{\text{R}}$ in Eq. (28) is the same as in the previous section. However, there is an important correction in $\tilde{\mathbf{q}}_{\text{R}}$ for the long-range scatters with $W_- \neq 0$. To elucidate the difference between short-range and long-range scatters, we perform an explicit calculation of $\Xi_{\text{T}}^{\alpha\beta}(\omega; q)$ and $\tilde{\Xi}_{\text{T}}^{\alpha\beta}(\omega; q)$ given by Eqs. (A3) and (A4), respectively. The transverse conductivity $\sigma_T(q)$ is obtained from evaluating Eq. (42) together with Eqs. (37) and (38).

Figure 5(a) shows the q dependence of transverse conductivity at $T = 0$ K and $E_F/E_c = 10^{-2}$ for short-range and long-range scatters. The behavior of $\sigma_T(q)$ is essentially identical for both cases at various disorder strengths. In the weak disorder regime ($W/W_c = 0.1$), it is peaked at $q = 0$ and converges to zero near $q = 2k_F$. The long-ranged scatters shows a longer tail at $q > 2k_F$ than the short-ranged scatters due to the shift

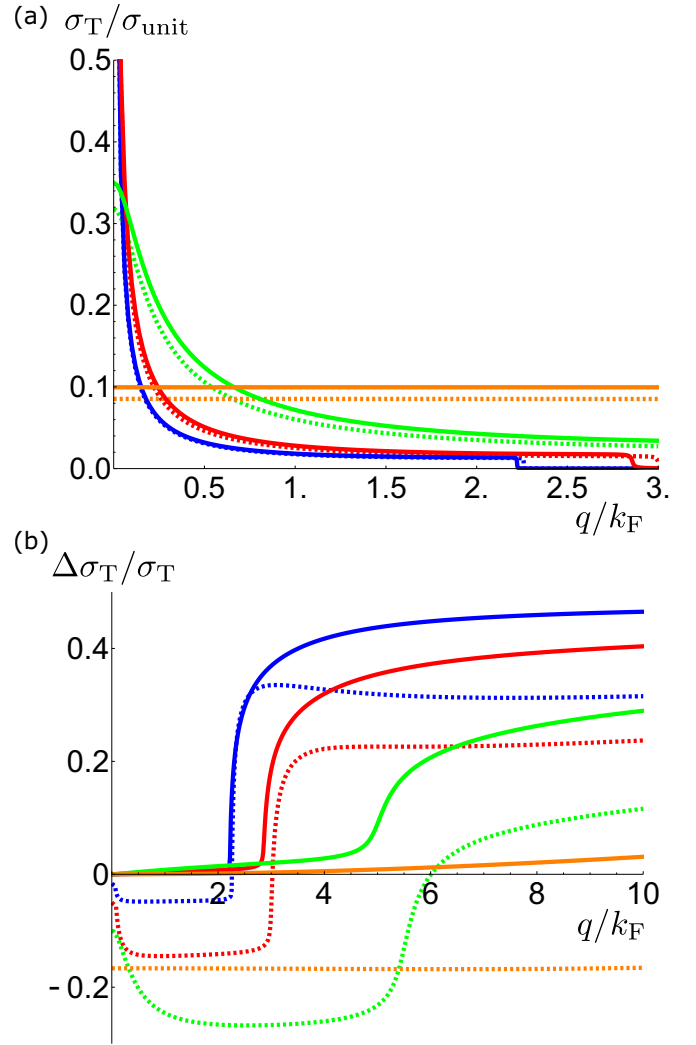


FIG. 5. Plot of (a) the transverse conductivity $\sigma_T(q)$ and (b) the ratio $\Delta\sigma_T/\sigma_T$ at $T = 0$ and $E_F/E_c = 10^{-2}$ for short-range scatters (solid lines) and long-ranged scatters (dashed lines). The disorder strength is taken at $W/W_c = 0.1$ (blue), 0.3 (red), 0.6 (green), and 1.0 (orange) from (a) bottom and (b) top.

in q by $Z_{\text{L}}^{\text{R}}(\omega)$. As the impurity strength is increased, the sharp peak at $q = 0$ is broadened and it acquires a longer tail for $q > 2k_F$. At the QCP ($W/W_c = 1.0$), the transverse conductivity becomes constant for $q \ll k_c$. In this regime, the negative contribution of the vertex correction results in the smaller transverse conductivity for the long-ranged scatters at $q \sim k_F$.

Second, we consider the q dependence of the vertex correction. The transverse conductivity is separated into the contribution from the bare vertex ($\Gamma_i = \sigma_i$) and the full vertex function

$$\sigma_T(q) = \sigma_T^{(0)}(q) + \Delta\sigma_T(q), \quad (46)$$

where the transverse conductivity with the bare vertex is given by

$$\begin{aligned} \sigma_T^{(0)}(q) &= \sigma_{\text{unit}} \int_{-\infty}^{\infty} d\omega \left(-\frac{\partial n_F(\omega)}{\partial \omega} \right) \\ &\times \text{Re} \left[\Xi_{\text{T}}^{\text{RA}}(\omega; q) - \Xi_{\text{T}}^{\text{RR}}(\omega; q) \right]. \end{aligned} \quad (47)$$

In Fig. 5(b), the ratio $\Delta\sigma_T/\sigma_T$ is plotted for short-range scatters and long-range scatters, respectively. For the short-ranged scatters, the vertex correction vanishes at $q = 0$. This is because $\Gamma_T^{\text{RA/RR}}(q) = 1$ for the short-ranged scatters and $\tilde{\Xi}_T^{\text{RA/RR}}(\omega; q = 0) = 0$. Also, the effect of positive contributions for $q > 2k_F$ is limited as the transverse conductivity is vanishingly small. At the QCP, the vertex correction is negligible for $q \ll k_c$. In contrast, the vertex correction is important for the long-ranged scatters, showing negative contributions as the disorder strength is increased. At the QCP, the vertex correction accounts for approximately -20% of σ_T for $q \ll k_c$.

IV. NUCLEAR SPIN-LATTICE RELAXATION RATE

As mentioned in Sec. I, the nuclear spin-lattice relaxation rate $1/T_1$ due to orbital currents is generally related to the real part of the dynamical transverse conductivity $\sigma_T(q, \omega_0)$ with the nuclear Larmor frequency ω_0 . It is, however, noted that the present systems with disorder have a finite damping rate $1/\tau(\omega) = -2\text{Im}[\Sigma^R(\omega)]$. For $\omega_0\tau(\omega_0) \ll 1$, the dynamical conductivity can be approximated by the static conductivity as $\text{Re}\sigma_T(q, \omega_0) \approx \sigma_T(q)$. From Eq. (1), the nuclear spin-lattice relaxation rate is given by

$$\frac{\hbar}{T_1 k_B T} = \frac{2\gamma_n^2 \mu_0^2 \hbar}{3\pi^2} \int_0^\infty dq \sigma_T(q) \frac{q_c^2}{q^2 + q_c^2}, \quad (48)$$

where we introduce a smooth cutoff procedure with $q_c = 2k_c$. By substituting Eq. (48) for $\sigma_T(q)$, we compute $(T_1 T)^{-1}$ for the disordered Weyl fermion systems and elucidate its critical behavior near the QCP.

A. Numerical results

In the previous section, we have shown that the difference between the short-ranged and long-ranged scatters on $\sigma_T(q)$ is resulted from the self-energy and the vertex correction. To confirm that it does not affect the critical behavior, we compare the nuclear spin-lattice relaxation rate for both cases at $T = 0$. In the following, the parameters are fixed as $E_c = 1.0$ eV, $c^* = 10^4$ m/s, and $\gamma_n = 267.5 \times 10^6 \text{ s}^{-1} \text{ T}^{-1}$.

In Fig. 6(a), the nuclear spin-lattice relaxation rate is plotted as a function of the Fermi energy at $T = 0$. While there is no significant difference in $(T_1 T)^{-1}$ between the short-ranged and long-ranged scatters below the QCP, their difference becomes visible above the QCP. At the QCP, $(T_1 T)^{-1}$ is proportional to E_F for both scatters for small E_F . The small difference between the short-ranged and long-ranged scatters results from the cancellation of the negative vertex correction by the self-energy correction $Z_L^R(\omega)$ after performing the integration. In addition to the energy dependence, the nuclear spin-lattice relaxation rate scales with the disorder strength, as shown in Fig. 6(b). We find that $(T_1 T)^{-1}$ is proportional to $(W - W_c)^2$ in the limit of $E_F = T = 0$, although it deviates from the quadratic dependence away from the QCP.

Since the critical behavior is the same for both the short-ranged and long-ranged scatters, we consider the nuclear spin-lattice relaxation rate under the long-ranged scatters at finite temperatures. First, the nuclear spin-lattice relaxation rate at $E_F = 0$ is considered. In this case, the chemical potential does

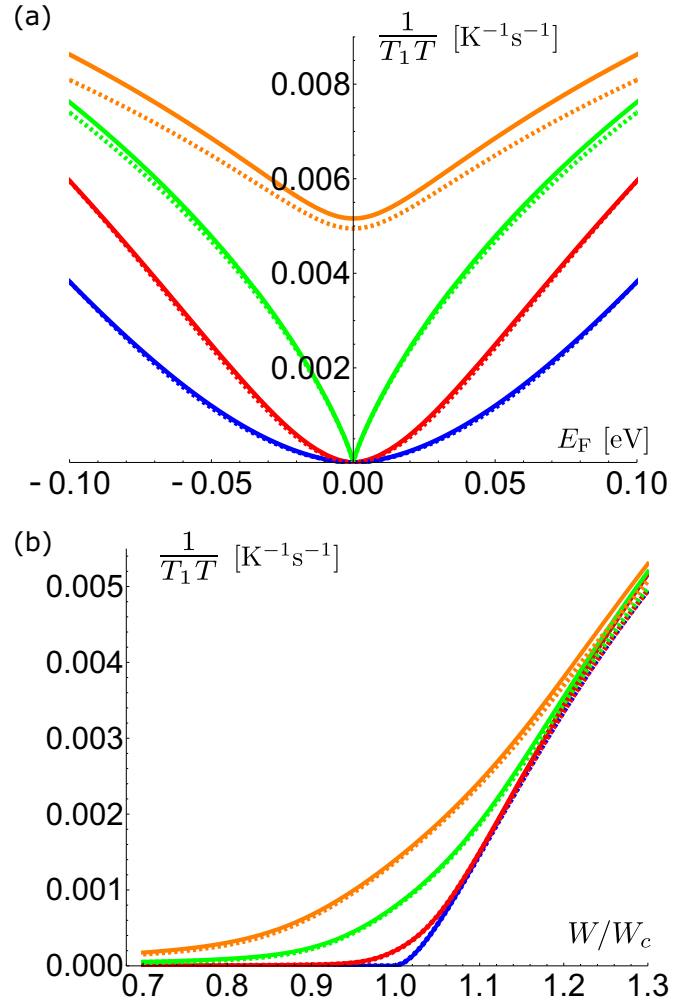


FIG. 6. The nuclear spin-lattice relaxation rate $(T_1 T)^{-1}$ at $T = 0$ (a) against the Fermi energy and (b) against the disorder strength for short-range scatters (solid lines) and long-ranged scatters (dashed lines). In (a), the disorder strength is taken at $W/W_c = 0.4$ (blue), 0.7 (red), 1.0 (green), and 1.3 (orange) from bottom. In (b), the Fermi energy is taken at $E_F = 0$ (blue), 1 meV (red), 5 meV (green), and 10 meV (orange) from bottom.

not depend on the temperature. In Fig. 7(a), we plot $(T_1 T)^{-1}$ as a function of temperatures for different impurity strengths, which shows the critical behavior of the nuclear spin-lattice relaxation rate. As the impurity strength increases, the transition from $(T_1 T)^{-1} \propto T^2$ to T occurs at lower temperatures. At the QCP, the nuclear spin-lattice relaxation rate is linearly proportional to the temperature from $T = 0$. Above the QCP, the density of states at the Weyl point becomes finite, so $(T_1 T)^{-1}$ becomes roughly constant.

Second, we consider the nuclear spin-lattice relaxation rate for $E_F \neq 0$. In Fig. 7(b), we present the temperature dependence of $(T_1 T)^{-1}$ at $E_F = 10$ meV. At low temperatures, $(T_1 T)^{-1}$ is constant regardless of the impurity strength. For $k_B T \sim \mu(T) \sim E_F/2$, $(T_1 T)^{-1}$ initially shows a decrease followed by an increase with the strong temperature dependence. This upturn in $(T_1 T)^{-1}$ is caused by the shift in chemical potential [18]. Above $k_B T \sim E_F/2$, it shows the transition

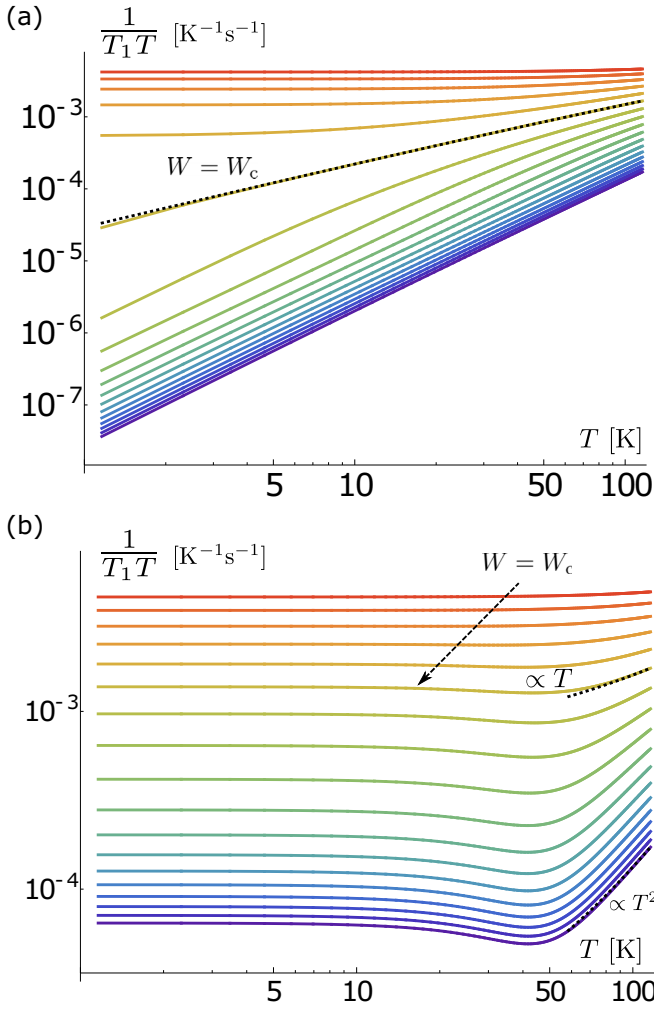


FIG. 7. The nuclear spin-lattice relation rate $(T_1T)^{-1}$ against temperatures for long-ranged scatters (a) at $E_F = 0$ and (b) $E_F = 10$ meV, respectively. The impurity strength W is taken between 0.4 and 1.3 with increase by 0.05. In (a), the dashed line represents the asymptotic expression Eq. (61) with $C_1 = 4.0$ and $C_2 = 3.8$.

from the T^2 dependence for weakly disordered systems to the T -linear behavior at the QCP.

Our result shows that the temperature dependence of $(T_1T)^{-1}$ reflects the scaling property at the disorder-induced QCP for small E_F . This is clearly illustrated in the temperature-disorder phase diagram (Fig. 8). The color code represents the exponent $\kappa(T)$ of the temperature in $(T_1T)^{-1}$ at $E_F = 0$, which is estimated as

$$\kappa(T) = - \lim_{\Delta T \rightarrow 0} \frac{\ln T_1T|_{T+\Delta T} - \ln T_1T|_T}{\ln(T + \Delta T) - \ln T}. \quad (49)$$

Below the QCP, $(T_1T)^{-1}$ is roughly described by the quadratic function with respect to T for a wide range of temperatures (regime II). Only in a narrow region near the QCP is the linear dependence in the temperature found (regime I). Above the QCP, the finite density of states leads to the constant value of $(T_1T)^{-1}$ (regime III).

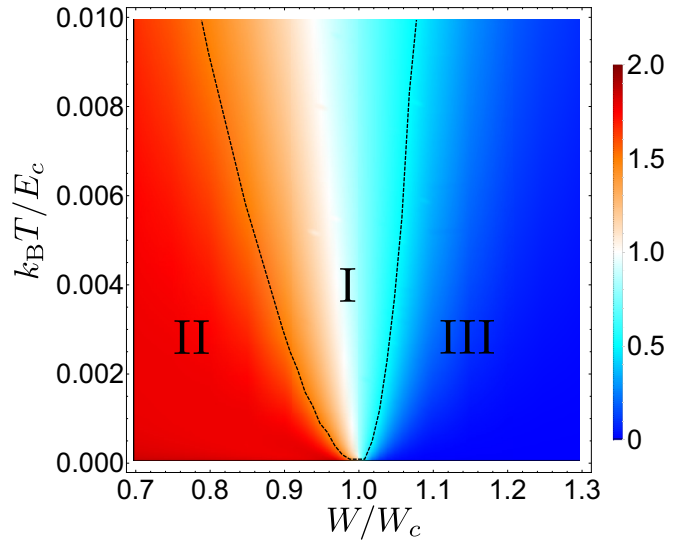


FIG. 8. Temperature-disorder phase diagram obtained by the SCBA. The color code indicates the exponent of $(T_1T)^{-1}$ with respect to the temperature at $E_F = 0$, defined as $\kappa(T)$ in the main text. The boundary between three regimes is estimated from $\kappa(T)$ (dashed line).

B. Asymptotic expressions

From the numerical calculation, $(T_1T)^{-1}$ is shown to be linear in the temperature near the QCP. To extract the exact temperature dependence, we derive the expression for the short-ranged scatters without the vertex correction, which is written as

$$\frac{\hbar}{T_1 k_B T} = \frac{2\gamma_n^2 \mu_0^2 E_c}{3\pi^2 c^*} \int_{-\infty}^{\infty} d\omega \left(-\frac{\partial n_F(\omega)}{\partial \omega} \right) \int_0^{\infty} dQ \sigma_T^{(0)}(q),$$

with the expression for $\sigma_T^{(0)}(q)$ given in Eq. (47) and $Q = q/k_c$. We should note that the scaling of $(T_1T)^{-1}$ at the QCP is not affected by the vertex correction and the additional self-energy correction $Z_L^R(\omega)$. This is confirmed by comparing the obtained expression with the numerical results.

For convenience, we shift Kx by $Kx + \frac{Q}{2}$ in $I_n^{\alpha\beta}(K)$ of Eq. (A3) and introduce new integration variables K' and x' . The transverse component is rewritten as

$$\begin{aligned} \Xi_T^{\alpha\beta}(\omega; q) = & \int_0^{\infty} \frac{K^2 dK}{1+K^2} \int_0^{\infty} \frac{K'^2 dK'}{1+K'^2} [\tilde{\Omega}_\alpha \tilde{\Omega}_\beta I_{0,0}^{\alpha\beta}(K, K') \\ & - I_{2,0}^{\alpha\beta}(K, K') - Q I_{1,0}^{\alpha\beta}(K, K')] \\ & \times \delta(Kx - K'x' + Q). \end{aligned} \quad (50)$$

Here, the expressions for the integrals are defined as

$$\begin{aligned} I_{n,m}^{\alpha\beta}(K, K') = & K^n K^m \int_{-1}^1 x^n dx \int_{-1}^1 x'^m dx' \\ & \times \frac{\delta[K^2(1-x^2) - K'^2(1-x'^2)]}{(\tilde{\Omega}_\alpha^2 - K^2)(\tilde{\Omega}_\beta^2 - K'^2)}. \end{aligned} \quad (51)$$

Taking the integration over Q , the second term is canceled out by the third term and we obtain

$$\int_0^\infty dQ \Xi_T^{\alpha\beta}(\omega; q) = \int_0^\infty \frac{K^2 dK}{1+K^2} \int_K^\infty \frac{K'^2 dK'}{1+K'^2} \times \tilde{\Omega}_\alpha \tilde{\Omega}_\beta I_{0,0}^{\alpha\beta}(K, K'), \quad (52)$$

where

$$I_{0,0}^{\alpha\beta}(K, K') = \frac{2 \text{Arcsinh}\left(\frac{K}{\sqrt{K'^2 - K^2}}\right)}{KK'(\tilde{\Omega}_\alpha^2 - K^2)(\tilde{\Omega}_\beta^2 - K'^2)}. \quad (53)$$

1. Weak disorder

In the weak disorder regime ($W \ll W_c$), the imaginary part of the Green's function $G(\mathbf{k}, \omega)$ is strongly peaked around $\hbar c^* k = \hbar \omega$ with its width proportional to the imaginary part of the self-energy. Thus, we can simplify the integral by introducing the Dirac delta function $-\pi \text{Im}[\tilde{\Omega}_R] \delta(K' - \text{Re}[\tilde{\Omega}_R])$, where $\tilde{\omega}_R = \omega + \frac{i}{2\tau}$. Under this approximation, the leading order term is obtained as

$$\int_0^\infty dQ \Xi_T^{\alpha\beta}(\omega; q) = \frac{\pi \text{Re}[\tilde{\Omega}_R] \text{Im}[\tilde{\Omega}_R] \tilde{\Omega}_\alpha \tilde{\Omega}_\beta}{16(\tilde{\Omega}_\beta^2 - \omega^2)} \times (\pi + 2i \ln |\omega| \tau)^2. \quad (54)$$

We should note that the above integral is convergent in the limit of the infinite momentum cutoff. This is expected as the momentum cutoff is not necessary for a clean system. Substituting the above expression, the nuclear spin-lattice relaxation rate is derived as

$$\frac{\hbar}{T_1 k_B T} = \frac{\gamma_n^2 \mu_0^2 e^2}{6\pi^3 c^{*2}} \int_{-\infty}^\infty d\omega \left(-\frac{\partial n_F(\omega)}{\partial \omega} \right) \omega^2 \ln |\omega| \tau. \quad (55)$$

For a Weyl electron system without disorder, $(T_1 T)^{-1} \propto T^2 \ln(2k_B T / \hbar \omega_0)$ with ω_0 denoting the nuclear Larmor frequency [19,20,28]. In Eq. (55), the nuclear Larmor frequency is replaced with the scattering rate $\frac{1}{2\tau} = \text{Im}[\tilde{\omega}_R] = \frac{W}{W_c} \frac{\hbar \omega^2}{E_c}$. The equivalent result was obtained in metallic systems [33]. At $\mu = 0$, it is derived as

$$\frac{\hbar}{T_1 k_B T} = 2\pi \left(\frac{\gamma_n \mu_0 e k_B T}{6\pi \hbar c^*} \right)^2 \left(\ln \frac{2E_c W_c}{k_B T W} - 1.05 \right). \quad (56)$$

Thus, the T^2 dependence of $(T_1 T)^{-1}$ holds under weak disorder. However, the logarithmic term is different from the clean system as the temperature T appears in the denominator.

2. QCP

The SCBA solution at the QCP ($W = W_c$) is given by $\tilde{\omega}_R = \sqrt{\frac{E_c \omega}{2\hbar}} (1 + i)$ for small ω . In this case, we cannot simplify the integral by assuming the small imaginary part in the self-energy. After evaluating the integral over K and K' , the leading order term is obtained as

$$\int_0^\infty dQ \Xi_T^{\text{RA}}(\omega; q) = \frac{\pi^2 \omega^2 \tau^2}{8} \left[-C_1 - C_2 \ln \omega \tau + \frac{i\pi}{2} + \ln 2 \right], \quad (57)$$

$$\int_0^\infty dQ \Xi_T^{\text{RR}}(\omega; q) = \frac{i\pi^2 \omega^2 \tau^2}{8} [-C_1 - C_2 \ln \omega \tau + i\pi - \ln 2]. \quad (58)$$

Here, there is a diverging term in the integral, so we need a momentum cutoff for convergence. Since it was not possible to obtain a simple analytical form of the diverging term, the coefficients were estimated as $C_1 = 1.75$ and $C_2 = 4.0$ by the numerical fitting. The integral of nondiverging terms is evaluated without the cutoff. The nuclear spin-lattice relaxation rate is derived as

$$\frac{\hbar}{T_1 k_B T} = \frac{e^2 \gamma_n^2 \mu_0^2 E_c}{24\pi^3 \hbar c^{*2}} \int_{-\infty}^\infty d\omega \left(-\frac{\partial n_F(\omega)}{\partial \omega} \right) \times |\omega| (\pi + \ln 2 - C_1 - C_2 \ln \omega \tau). \quad (59)$$

Substituting $\frac{1}{2\tau} = \text{Im}[\tilde{\omega}_R] = \sqrt{\frac{E_c \omega}{2\hbar}}$, the expression for $\mu = 0$ is obtained as

$$\frac{\hbar}{T_1 k_B T} = \frac{\pi E_c k_B T \ln 2}{24} \left(\frac{e \gamma_n \mu_0}{\pi \hbar c^*} \right)^2 \times C_2 \left(\ln \frac{2E_c}{k_B T} - \frac{2C_1}{C_2} - 0.653 + \frac{2\pi + 2 \ln 2}{C_2} \right). \quad (61)$$

Therefore, $(T_1 T)^{-1}$ is proportional to $T \ln \frac{E_c}{k_B T}$ with the constants C_1 and C_2 dependent on the choice of momentum cutoff. In Fig. 7(a), Eq. (61) is plotted with $C_1 = 4.0$ and $C_2 = 3.8$ (dashed line), which is in good agreement with the numerical result. Therefore, the temperature dependence of $(T_1 T)^{-1}$ at the QCP is correctly described by Eq. (61).

C. Scaling of $(T_1 T)^{-1}$ near the QCP

The scaling of the conductivity with the system size (L) is derived as $\sigma \sim L^{2-d}$ in a d -dimensional system [52,53]. This is also obtained from the RG analysis [36]. Since the transverse conductivity is integrated over q , we obtain

$$\frac{\hbar}{T_1 k_B T}(\delta, \Omega) = L^{1-d} G\left(\frac{L}{\delta^{-\nu}}, \frac{\Omega}{\delta^{\nu z}}\right) = \delta^{(d-1)\nu} F\left(\frac{L}{\delta^{-\nu}}, \frac{\Omega}{\delta^{\nu z}}\right), \quad (62)$$

where G and F are the universal scaling functions, $\delta = W/W_c - 1$ and $\Omega = \max[\mu(T), k_B T]/E_c$.

At the QCP ($\delta = 0$), the expression for $(T_1 T)^{-1}$ should be independent of δ . Thus, it is scaled as

$$\frac{\hbar}{T_1 k_B T}(\delta = 0, \Omega) \sim \Omega^{\frac{d-1}{z}}. \quad (63)$$

Above the QCP, the nuclear spin-lattice relaxation rate becomes finite even at a Weyl point. At $\Omega = 0$, it is given by

$$\frac{\hbar}{T_1 k_B T}(\delta > 0, \Omega = 0) \sim \delta^{(d-1)\nu}. \quad (64)$$

Given $z = 2$ and $d = 3$ for the SCBA, we obtain $(T_1 T)^{-1} \sim T$ at the QCP. Therefore, the scaling analysis is consistent with the present result within the SCBA. In this special case, the nuclear spin-lattice relaxation rate is proportional to the square of density of states. Generally, there is no simple relationship between the orbital contribution of $(T_1 T)^{-1}$ and the density of states at the QCP. On the other hand, the critical exponents are obtained as $z = 1.5$ and $\nu = 1$ in the one-loop RG calculation [49]. The numerical calculations of the critical exponents were also performed, yielding $z \approx 1.5$ and $\nu \approx 1$ [51,55]. Substituting $z = 1.5$, we predict $(T_1 T)^{-1} \sim T^{\frac{4}{3}}$ at the QCP. Thus, there is no significant difference from the SCBA result except for a slight modification in the exponent.

V. PARTICLE-HOLE ASYMMETRY

While the particle-hole symmetry is conserved in the SCBA, higher order perturbations break this symmetry. In this section, we discuss the effect of particle-hole asymmetry with the the SCTA, which takes account of characteristic higher order corrections with respect to impurity potential u_{ab} .

A. Critical exponents in the SCTA

The self-consistent equation for the SCTA is given by

$$\Sigma_a^R(\omega) = \frac{n_i |u_{aa}|}{\hbar} \left(1 - \sum_{b=\mathcal{L},\mathcal{R}} \frac{|u_{ab}|}{\hbar} \sum_{\mathbf{k}} G_b^R(\mathbf{k}, \omega) \right)^{-1}, \quad (65)$$

where the subscript a denotes the chirality. We define the impurity concentration and impurity potential as $\bar{n}_i = a_c^3 n_i$ and $\bar{u} = (|u_{\mathcal{L}\mathcal{L}}| + |u_{\mathcal{R}\mathcal{L}}|)/a_c^3 E_c$, where the effective lattice constant $a_c = 2\pi/k_c$ is introduced. Similarly to the SCBA, the self-energy has an identity matrix element satisfying

$$\Sigma_{\text{SCTA}}(\omega) = \frac{\bar{n}_i \bar{u}}{\hbar(1 - 4\pi \bar{u} \tilde{\Omega}^R f(\omega))}, \quad (66)$$

with the expression of $f(\omega)$ given in Eq. (9) and $\tilde{\Omega}^R = \hbar \tilde{\omega}_R / E_c$. Here, the chemical potential is shifted so $\tilde{\omega}_R = \omega + (\mu + \bar{n}_i \bar{u} E_c) / \hbar - \Sigma_1^R(\omega)$. We should note that the impurity concentration \bar{n}_i needs to be small for justifying the SCTA. For long-ranged disorder, the impurity concentration is multiplied by $\frac{1}{2}$. The self-consistent solution is derived as

$$\tilde{\Omega}^R = \frac{1}{2} \left(\Omega + \frac{\delta}{(2\pi \bar{u}^2 - i)} \pm \frac{\sqrt{4\Omega(2\pi \bar{u}^2 - i) + [\Omega(2\pi \bar{u}^2 - i) + \delta]^2}}{(2\pi \bar{u}^2 - i)} \right), \quad (67)$$

where $\delta = \bar{n}_i / \bar{n}_c - 1$. Similar to the SCBA, the critical impurity concentration is defined at which the imaginary part of the self-energy becomes finite. At the QCP ($\bar{n}_c = W_c / 4\pi \bar{u}^2$), the solution for $\Omega \ll 1$ is given by

$$\tilde{\Omega}^R = \sqrt{\frac{2\Omega}{-2i + \pi \bar{u}}}. \quad (68)$$

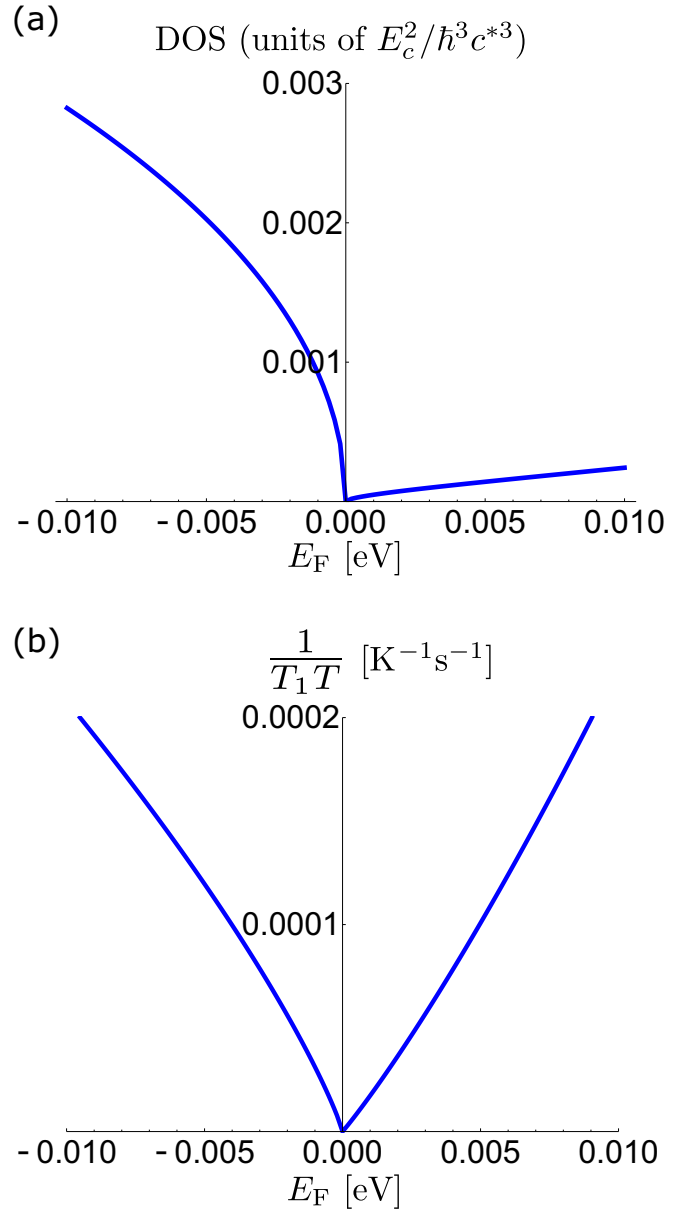


FIG. 9. (a) The density of states and (b) the nuclear spin-lattice relaxation rate $(T_1 T)^{-1}$ at $T = 0$ are plotted against the Fermi energy E_F at the QCP. For both plots, the impurity potential is fixed at $\bar{u} \approx 0.6$. The other parameters are the same as in Fig. 6.

Above the QCP at $\Omega = 0$, it is given by

$$\tilde{\Omega}^R = \frac{2\delta(\pi \bar{u} + 2i)}{4 + \pi \bar{u}^2}. \quad (69)$$

Thus, the critical exponents are identical with the SCBA ($z = 2$, $\nu = 1$). In the limit of $\bar{u} \rightarrow 0$, Eq. (67) turns into the solution for the SCBA.

Using the solution for the SCTA, we study the critical behavior under the strong impurity potential. The impurity potential is fixed at $\bar{u} \approx 0.6$, giving the critical impurity concentration $\bar{n}_c \approx 0.14$. In Fig. 9(a), the density of states against the Fermi energy is calculated at the QCP. The difference from the SCBA is that the density of states is not symmetric about

the Weyl point. Thus, the particle-hole symmetry is broken under the strong impurity potential, although the square root singularity is still obtained at the QCP. Above the QCP, the density of states at the Weyl point is suppressed by \bar{u}^2 in the denominator of Eq. (69). We also confirm that the nuclear spin-lattice relaxation rate is linearly proportional to the temperature at the QCP as in the SCBA. This is illustrated in Fig. 9(b), showing the linear dependence of $(T_1 T)^{-1}$ with respect to the Fermi energy at $T = 0$ for small E_F . Here, we ignore the vertex correction and the q -dependent self-energy for simplicity.

B. Enhanced upturn in $(T_1 T)^{-1}$

In the previous section, we show that the higher order contributions in impurity scattering result in the particle-hole symmetry breaking. This is particularly important at finite temperatures, as it modifies the temperature dependence of the chemical potential. We should note that the particle-hole symmetry is recovered in the unitary limit as we can ignore unity in the denominator of Eq. (66) in the limit of $\bar{u} \rightarrow \infty$ [60].

Within the SCBA that preserves the particle-hole symmetry, the chemical potential moves toward Weyl points. Under strong impurity potential, this behavior is significantly modified to compensate for the imbalance of the density of states. In Fig. 10(a), the chemical potential is plotted against temperatures at $E_F = \pm 10$ meV. As the density of states is larger for $E_F < 0$ [Fig. 9(a)], the chemical potential tends to increase with the temperature. This results in an upturn of $\mu(T)$ for $E_F > 0$ and a reverse of the sign for $E_F < 0$. The important point is that the shift of $\mu(T)$ at low temperatures is strongly enhanced for $E_F < 0$ compared to the clean limit.

As discussed in Sec. IV A, the nuclear spin-lattice relaxation rate $(T_1 T)^{-1}$ shows the upturn at $k_B T \sim E_F/2$ due to the shift of chemical potential toward the Weyl point. Under the strong impurity potential, the overshooting of $\mu(T)$ above the Weyl point may happen as a result of the particle-hole asymmetry. This leads to the enhancement in the upturn of $(T_1 T)^{-1}$. In Fig. 10(b), the low-temperature behavior of $(T_1 T)^{-1}$ is shown at $E_F = -10$ meV and $\bar{n}_i/\bar{n}_c = 0.3$. We find that it drops by half from $T = 0$ to $T \sim 40$ K before the uprising of the T^2 term, which is much larger than the upturn of $(T_1 T)^{-1}$ in a clean system.

VI. DISCUSSION

In this section, we discuss the recent NQR experiment of TaP, where $(T_1 T)^{-1}$ shows a T^2 behavior above $T^* = 30$ K and a $T^{-1/2}$ behavior (or an upturn) below T^* [17]. This experiment is for a pure sample and thus the strength of disorder should be much weaker than the critical strength (regime II). While the high temperature T^2 behavior was explained by the relaxation due to orbital currents in the Weyl nodes [17,19], there are two scenarios for the origin of the low-temperature upturn.

The first scenario is the conventional Korringa process of parabolic bands ($E \propto k^2$) which are related to neither the Weyl

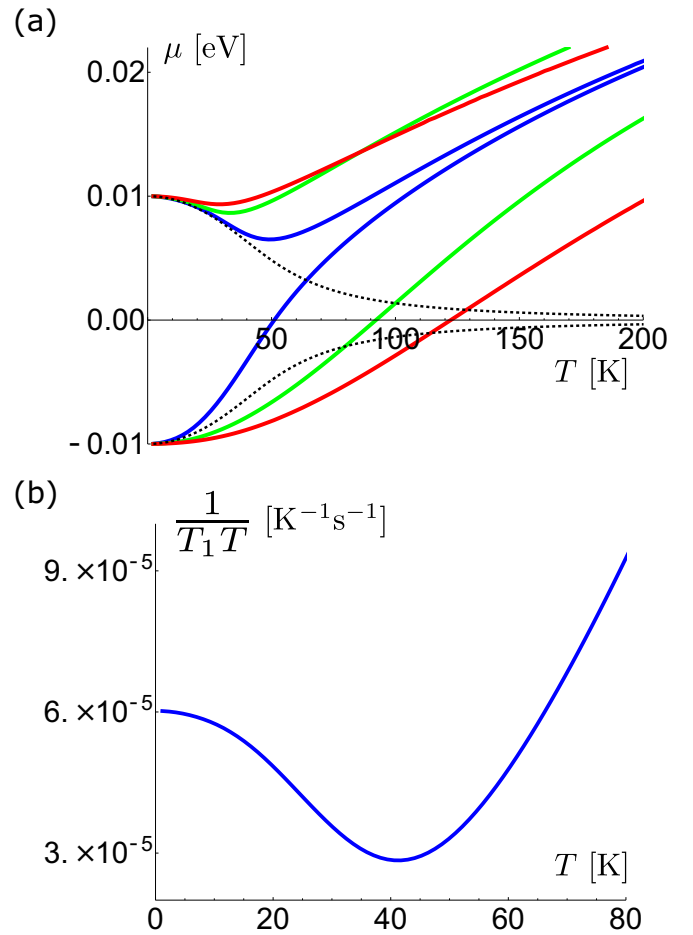


FIG. 10. (a) Chemical potential against temperatures within the SCTA for $E_F = \pm 10$ meV. The impurity concentration is set at $\bar{n}_i/\bar{n}_c = 0.3$ (blue), 0.6 (green), 0.9 (red) from the Weyl point. The dashed lines show the result of clean systems. (b) Plot of $(T_1 T)^{-1}$ at low temperatures for $\bar{n}_i/\bar{n}_c = 0.3$ and $E_F = -10$ meV.

nodes nor linear bands ($E \propto k$). In Ref. [17], the origin of the upturn was speculated to be correlation among electrons in the parabolic bands. Since the impurity effect only results in the broadening of parabolic bands, the low-temperature upturn is expected to be almost unchanged even if a small amount of impurities is introduced in this scenario.

On the other hand, the low-temperature upturn might originate from temperature dependence of the chemical potential $\mu(T)$ associated with the presence of the Weyl node. However, $\mu(T)$ arising from an ideal Weyl band structure leads to an upturn which is too small to explain the experiment. Okvátovity *et al.* postulated that the entire band structures of TaP alters $\mu(T)$ to enhance the upturn and proposed a phenomenological model of chemical potential to reach a good agreement between theory and experiment [18,62].

To observe the impurity effect, further research is required with the controlled doping. From the result in Sec. V B, we predict that the impurity effect on the low-temperature upturn could become significant even below the critical impurity strength.

TABLE I. The scaling relation of the nuclear spin-lattice relaxation rate $(T_1 T)^{-1}$. We denote the characteristic energy as $E = \max[k_B T, \mu(T)]$ and the impurity strength $\delta = W/W_c - 1$.

	SCBA and SCTA	Scaling ansatz
Regime I	$E \ln 1/E$	$E^{\frac{2}{z}}$
Regime II	$E^2 \ln 1/E$	E^2
Regime III	δ^2	$\delta^{2\nu}$

VII. CONCLUSION

We have studied the nuclear spin-lattice relaxation rate due to orbital currents in disordered Weyl fermion systems, employing the SCBA. In this paper, two types of the disorder potential were considered, namely, the short-ranged (intervalley and intravalley scattering) and long-ranged scatters (only intravalley scattering). For both cases, it shows the critical behavior with the critical exponents $z = 2$ and $\nu = 1$ in the SCBA.

The orbital contribution of the nuclear spin-lattice relaxation rate is determined by the transverse conductivity, whose wave-vector dependence was investigated under disorder. The vertex correction was obtained in a gauge-invariant manner for general wave vector q , using the conserving approximation for the SCBA. As shown in Fig. 5, the vertex correction has a negative contribution for the long-ranged scatters, while it vanishes at $q = 0$ for the short-ranged scatters.

Our main result is the scaling relation of the nuclear spin-lattice relaxation near the disorder-induced QCP. As shown in Fig. 8, we classified three different regimes from the temperature dependence of $(T_1 T)^{-1}$. For each regime, the scaling of the nuclear spin-lattice relaxation rate is summarized in Table I. Within the SCBA, we obtained the asymptotic expression at the QCP as $(T_1 T)^{-1} \sim T \ln(1/T)$. Although the critical exponents from the one-loop RG analysis predicts the exponent in $(T_1 T)^{-1}$ slightly greater than the SCBA result [49], our result provides a good physical picture near the disorder-induced QCP in Weyl fermion systems.

In addition, we discussed the effect of the particle-hole asymmetry, employing the SCTA. In regime II under the strong impurity potential, the temperature dependence of chemical potential is significantly modified from the particle-hole symmetric systems. As a result, the low temperature upturn in $(T_1 T)^{-1}$ becomes enhanced. Hence, the impurity effect could also play an important role in weakly disordered systems.

ACKNOWLEDGMENTS

We would like to thank I. Tateishi, V. Könye, H. Matsuura, and H. Yasuoka for helpful comments and discussions. This work was supported by Grants-in-Aid for Scientific Research from the Japan Society for the Promotion of Science (Grants No. JP18H01162 and No. JP18K03482). T.H. is supported by Japan Society for the Promotion of Science through Program for Leading Graduate Schools (MERIT) and JSPS KAKENHI (Grant No. 18J21985).

APPENDIX A: EXPRESSIONS FOR SELF-ENERGY CORRECTIONS

The explicit expressions for $\Xi_L^{\alpha\beta}(\omega; q)$, $\tilde{\Xi}_L^{\alpha\beta}(\omega; q)$, $\Xi_T^{\alpha\beta}(\omega; q)$, and $\tilde{\Xi}_T^{\alpha\beta}(\omega; q)$ are obtained as follows:

$$\begin{aligned} \Xi_L^{\alpha\beta}(\omega; q) = & \int_0^\infty \frac{K^2 dK}{1+K^2} \left[\left(\tilde{\Omega}_\alpha \tilde{\Omega}_\beta - \frac{1}{4} \tilde{Q}_\alpha \tilde{Q}_\beta - K^2 \right) \right. \\ & \times I_0^{\alpha\beta}(K) + \frac{1}{2} (\tilde{Q}_\alpha - \tilde{Q}_\beta) I_1^{\alpha\beta}(K) \\ & \left. + 2I_2^{\alpha\beta}(K) \right], \end{aligned} \quad (\text{A1})$$

$$\begin{aligned} \tilde{\Xi}_L^{\alpha\beta}(\omega; q) = & \int_0^\infty \frac{K^2 dK}{1+K^2} \left[\frac{1}{2} (\tilde{\Omega}_\alpha \tilde{Q}_\beta - \tilde{\Omega}_\beta \tilde{Q}_\alpha) I_0^{\alpha\beta}(K) \right. \\ & \left. + (\tilde{\Omega}_\alpha + \tilde{\Omega}_\beta) I_1^{\alpha\beta}(K) \right], \end{aligned} \quad (\text{A2})$$

$$\begin{aligned} \Xi_T^{\alpha\beta}(\omega; q) = & \int_0^\infty \frac{K^2 dK}{1+K^2} \left[\left(\tilde{\Omega}_\alpha \tilde{\Omega}_\beta + \frac{1}{4} \tilde{Q}_\alpha \tilde{Q}_\beta \right) I_0^{\alpha\beta}(K) \right. \\ & \left. - \frac{1}{2} (\tilde{Q}_\alpha - \tilde{Q}_\beta) I_1^{\alpha\beta}(K) - I_2^{\alpha\beta}(K) \right], \end{aligned} \quad (\text{A3})$$

$$\begin{aligned} \tilde{\Xi}_T^{\alpha\beta}(\omega; q) = & \int_0^\infty \frac{K^2 dK}{1+K^2} \left[\frac{1}{2} (\tilde{\Omega}_\alpha \tilde{Q}_\beta + \tilde{\Omega}_\beta \tilde{Q}_\alpha) I_0^{\alpha\beta}(K) \right. \\ & \left. + (\tilde{\Omega}_\alpha - \tilde{\Omega}_\beta) I_1^{\alpha\beta}(K) \right], \end{aligned} \quad (\text{A4})$$

where the integrals $I_n^{\alpha\beta}(K)$ for $n = 0, 1, 2$ are given by

$$\begin{aligned} I_n^{\alpha\beta}(K) = & K^n \int_{-1}^1 \frac{dx}{2} x^n \left(\tilde{\Omega}_\alpha^2 - \frac{1}{4} \tilde{Q}_\alpha^2 - K^2 + K \tilde{Q}_\alpha x \right)^{-1} \\ & \times \left(\tilde{\Omega}_\beta^2 - \frac{1}{4} \tilde{Q}_\beta^2 - K^2 - K \tilde{Q}_\beta x \right)^{-1}. \end{aligned} \quad (\text{A5})$$

In particular, $\tilde{\Xi}_L^{\text{RR}}(\omega; q) = 0$ because of $I_1^{\text{RR}}(K) = 0$. Here we introduce dimensionless variables $\tilde{\Omega}_\alpha$ and \tilde{Q}_α as

$$\tilde{\Omega}_\alpha = \frac{\hbar \tilde{\omega}_\alpha}{E_c} = \frac{\hbar \omega + \mu - \hbar \Sigma_1^\alpha(\omega; q/2)}{E_c}, \quad (\text{A6})$$

$$\tilde{Q}_\alpha = \frac{\tilde{q}_\alpha}{k_c} = Z_L^\alpha(\omega; q/2) \frac{q}{k_c}, \quad (\text{A7})$$

where $E_c = \hbar c^* k_c$.

APPENDIX B: APPROXIMATE SOLUTION FOR THE SELF-ENERGY CORRECTION

Here, we derive the q -dependent self-energy to conserve the gauge invariance. From Eqs. (23) and (27),

$$\Sigma_1^{\text{R}}(\omega; q/2) = W \tilde{\omega}_R f(\omega; q/2), \quad (\text{B1})$$

$$Z_L^{\text{R}}(\omega; q/2) - 1 = W \frac{2g(\omega; q/2) + \tilde{Q}_R f(\omega; q/2)}{2Q}, \quad (\text{B2})$$

where $\tilde{\omega}_R = \omega + \mu/\hbar - \Sigma_1^{\text{R}}(\omega; q/2)$, $Q = q/k_c$, and $\tilde{Q}_R = Z_L^{\text{R}}(\omega; q/2) \frac{q}{k_c}$. To solve the above self-consistent equations, we expand $f(\omega; q/2)$ and $g(\omega; q/2)$ for small q . This approximation is justified as we are interested in the integration of the transverse conductivity over q , which converges for $q \ll k_c$ under weak disorder. As the disorder strength is increased,

the transverse conductivity becomes constant with respect to q . Thus, the q dependence in the self-energy does not affect the integral for $q \sim k_c$. The dimensionless functions $f(\omega; q/2)$ and $g(\omega; q/2)$ for $q \ll k_c$ are given as

$$f(\omega; q/2) = \int_0^\infty \frac{K^2 dK}{K^2 + 1} \int_{-1}^1 \frac{dx}{2} \frac{1}{\tilde{\Omega}_R^2 - K^2 - K\tilde{Q}_R x - \frac{\tilde{Q}_R^2}{4}}$$

$$= -\frac{\pi}{2} \frac{1 + i\tilde{\Omega}_R}{1 + \tilde{\Omega}_R^2} + O(\tilde{Q}_R^2), \quad (\text{B3})$$

$$g(\omega; q/2) = \int_0^\infty \frac{K^2 dK}{K^2 + 1} \int_{-1}^1 \frac{dx}{2} \frac{Kx}{\tilde{\Omega}_R^2 - K^2 - K\tilde{Q}_R x - \frac{\tilde{Q}_R^2}{4}}$$

$$= \frac{\pi\tilde{Q}_R}{12} \frac{2 + i\tilde{\Omega}_R(3 + \tilde{\Omega}_R^2)}{(1 + \tilde{\Omega}_R^2)^2} + O(\tilde{Q}_R^3). \quad (\text{B4})$$

The solution of Eqs. (B1) and (B2) are given in Eqs. (44) and (45). In this approximation, the identity matrix element Σ_1^R is unchanged.

[1] N. P. Armitage, E. J. Mele, and A. Vishwanath, *Rev. Mod. Phys.* **90**, 015001 (2018).

[2] S.-M. Huang, S.-Y. Xu, I. Belopolski, C.-C. Lee, G. Chang, B. Wang, N. Alidoust, G. Bian, M. Neupane, C. Zhang, S. Jia, A. Bansil, H. Lin, and M. Z. Hasan, *Nat. Commun.* **6**, 7373 (2015).

[3] H. Weng, C. Fang, Z. Fang, B. A. Bernevig, and X. Dai, *Phys. Rev. X* **5**, 011029 (2015).

[4] S.-Y. Xu, I. Belopolski, D. S. Sanchez, C. Zhang, G. Chang, C. Guo, G. Bian, Z. Yuan, H. Lu, T.-R. Chang, P. P. Shibayev, M. L. Prokopyov, N. Alidoust, H. Zheng, C.-C. Lee, S.-M. Huang, R. Sankar, F. Chou, C.-H. Hsu, H.-T. Jeng, A. Bansil, T. Neupert, V. N. Strocov, H. Lin, S. Jia, and M. Z. Hasan, *Sci. Adv.* **1**, e1501092 (2015).

[5] B. Q. Lv, H. M. Weng, B. B. Fu, X. P. Wang, H. Miao, J. Ma, P. Richard, X. C. Huang, L. X. Zhao, G. F. Chen, Z. Fang, X. Dai, T. Qian, and H. Ding, *Phys. Rev. X* **5**, 031013 (2015).

[6] C. Shekhar, A. K. Nayak, Y. Sun, M. Schmidt, M. Nicklas, I. Leermakers, U. Zeitler, Y. Skourski, J. Wosnitza, Z. Liu, Y. Chen, W. Schnelle, H. Borrmann, Y. Grin, C. Felser, and B. Yan, *Nat. Phys.* **11**, 645 (2015).

[7] D. T. Son and B. Z. Spivak, *Phys. Rev. B* **88**, 104412 (2013).

[8] A. Burkov, *J. Phys.: Condens. Matter* **27**, 113201 (2015).

[9] F. Arnold, C. Shekhar, S.-C. Wu, Y. Sun, R. D. dos Reis, N. Kumar, M. Naumann, M. O. Ajeesh, M. Schmidt, A. G. Grushin, J. H. Bardarson, M. Baenitz, D. Sokolov, H. Borrmann, M. Nicklas, C. Felser, E. Hassinger, and B. Yan, *Nat. Commun.* **7**, 11615 (2016).

[10] X. Huang, L. Zhao, Y. Long, P. Wang, D. Chen, Z. Yang, H. Liang, M. Xue, H. Weng, Z. Fang, X. Dai, and G. Chen, *Phys. Rev. X* **5**, 031023 (2015).

[11] Z. Wang, Y. Zheng, Z. Shen, Y. Lu, H. Fang, F. Sheng, Y. Zhou, X. Yang, Y. Li, C. Feng, and Z.-A. Xu, *Phys. Rev. B* **93**, 121112(R) (2016).

[12] C.-L. Zhang, S.-Y. Xu, I. Belopolski, Z. Yuan, Z. Lin, B. Tong, G. Bian, N. Alidoust, C.-C. Lee, S.-M. Huang, T.-R. Chang, G. Chang, C.-H. Hsu, H.-T. Jeng, M. Neupane, D. S. Sanchez, H. Zheng, J. Wang, H. Lin, C. Zhang, H.-Z. Lu, S.-Q. Shen, T. Neupert, M. Z. Hasan, and S. Jia, *Nat. Commun.* **7**, 10735 (2016).

[13] R. Lundgren, P. Laurell, and G. A. Fiete, *Phys. Rev. B* **90**, 165115 (2014).

[14] A. Abragam, *Principles of Nuclear Magnetism* (Clarendon Press, Oxford, UK, 1961).

[15] T. Moriya, *J. Phys. Soc. Jpn.* **18**, 516 (1963).

[16] J. Korrying, *Physica* **16**, 601 (1950).

[17] H. Yasuoka, T. Kubo, Y. Kishimoto, D. Kasinathan, M. Schmidt, B. Yan, Y. Zhang, H. Tou, C. Felser, A. P. Mackenzie, and M. Baenitz, *Phys. Rev. Lett.* **118**, 236403 (2017).

[18] Z. Okvátovity, H. Yasuoka, M. Baenitz, F. Simon, B. Dóra, *Phys. Rev. B* **99**, 115107 (2019).

[19] Z. Okvátovity, F. Simon, and B. Dóra, *Phys. Rev. B* **94**, 245141 (2016).

[20] T. Hirotsawa, H. Maebashi, and M. Ogata, *J. Phys. Soc. Jpn.* **86**, 063705 (2017).

[21] A. Kobayashi, Y. Suzumura, and H. Fukuyama, *J. Phys. Soc. Jpn.* **77**, 064718 (2008).

[22] N. Tajima, R. Kato, S. Sugawara, Y. Nishio, and K. Kajita, *Phys. Rev. B* **85**, 033401 (2012).

[23] K. Kajita, Y. Nishio, N. Tajima, Y. Suzumura, and A. Kobayashi, *J. Phys. Soc. Jpn.* **83**, 072002 (2014).

[24] P. A. Wolff, *J. Phys. Chem. Solids* **25**, 1057 (1964).

[25] For a review, see Y. Fuseya, M. Ogata, and H. Fukuyama, *J. Phys. Soc. Jpn.* **84**, 012001 (2015).

[26] L. Wehrli, *Phys. Kondens. Mater.* **8**, 87 (1968).

[27] H. Fukuyama and R. Kubo, *J. Phys. Soc. Jpn.* **28**, 570 (1970).

[28] H. Maebashi, M. Ogata, and H. Fukuyama, *J. Phys. Soc. Jpn.* **86**, 083702 (2017).

[29] W. A. MacFarlane, C. B. L. Tschense, T. Buck, K. H. Chow, D. L. Cortie, A. N. Hariwal, R. F. Kiefl, D. Koumoulis, C. D. P. Levy, I. McKenzie, F. H. McGee, G. D. Morris, M. R. Pearson, Q. Song, D. Wang, Y. S. Hor, and R. J. Cava, *Phys. Rev. B* **90**, 214422 (2014).

[30] P. Lee and N. Nagaosa, *Phys. Rev. B* **43**, 1223 (1991).

[31] B. Dóra and F. Simon, *Phys. Rev. Lett.* **102**, 197602 (2009).

[32] H. Maebashi, T. Hirotsawa, M. Ogata, and H. Fukuyama, *J. Phys. Chem. Solids* **128**, 138 (2019).

[33] A. Knigavko, B. Mitrović, and K. V. Samokhin, *Phys. Rev. B* **75**, 134506 (2007).

[34] E. Fradkin, *Phys. Rev. B* **33**, 3257 (1986).

[35] E. Fradkin, *Phys. Rev. B* **33**, 3263 (1986).

[36] S. V. Syzranov, L. Radzihovsky, and V. Gurarie, *Phys. Rev. Lett.* **114**, 166601 (2015).

[37] S. V. Syzranov and L. Radzihovsky, *Annu. Rev. Condens. Matter Phys.* **9**, 35 (2018).

[38] S. V. Syzranov, V. Gurarie, and L. Radzihovsky, *Phys. Rev. B* **91**, 035133 (2015).

[39] R. Nandkishore, D. A. Huse, and S. L. Sondhi, *Phys. Rev. B* **89**, 245110 (2014).

[40] J. H. Pixley, David A. Huse, and S. Das Sarma, *Phys. Rev. X* **6**, 021042 (2016).

[41] Y. Ominato and M. Koshino, *Phys. Rev. B* **89**, 054202 (2014).

- [42] R. Shindou and S. Murakami, *Phys. Rev. B* **79**, 045321 (2009).
- [43] H. Shapourian and T. L. Hughes, *Phys. Rev. B* **93**, 075108 (2016).
- [44] B. Sbierski, G. Pohl, E. J. Bergholtz, and P. W. Brouwer, *Phys. Rev. Lett.* **113**, 026602 (2014).
- [45] J. H. Pixley, P. Goswami, and S. Das Sarma, *Phys. Rev. Lett.* **115**, 076601 (2015).
- [46] X. Luo, B. Xu, T. Ohtsuki, and R. Shindou, *Phys. Rev. B* **97**, 045129 (2018).
- [47] T. Louvet, D. Carpentier, and A. A. Fedorenko, *Phys. Rev. B* **94**, 220201(R) (2016).
- [48] P. Hosur, S. A. Parameswaran, and A. Vishwanath, *Phys. Rev. Lett.* **108**, 046602 (2012).
- [49] P. Goswami and S. Chakravarty, *Phys. Rev. Lett.* **107**, 196803 (2011).
- [50] C.-Z. Chen, J. Song, H. Jiang, Q.-F. Sun, Z. Wang, and X. C. Xie, *Phys. Rev. Lett.* **115**, 246603 (2015).
- [51] S. Bera, J. D. Sau, and B. Roy, *Phys. Rev. B* **93**, 201302(R) (2016).
- [52] B. Roy, V. Juričić, and S. D. Sarma, *Sci. Rep.* **6**, 32446 (2016).
- [53] B. Roy, R.-J. Slager, and V. Juričić, *Phys. Rev. X* **8**, 031076 (2018).
- [54] K. Kobayashi, T. Ohtsuki, and K.-I. Imura, *Phys. Rev. Lett.* **110**, 236803 (2013).
- [55] K. Kobayashi, T. Ohtsuki, K.-I. Imura, and I. F. Herbut, *Phys. Rev. Lett.* **112**, 016402 (2014).
- [56] N. H. Shon and T. Ando, *J. Phys. Soc. Jpn.* **67**, 2421 (1998).
- [57] M. Koshino and T. Ando, *Phys. Rev. B* **75**, 235333 (2007).
- [58] Y. Arimura and T. Ando, *J. Phys. Soc. Jpn.* **81**, 024702 (2012).
- [59] I. L. Aleiner and K. B. Efetov, *Phys. Rev. Lett.* **97**, 236801 (2006).
- [60] P. M. Ostrovsky, I. V. Gornyi, and A. D. Mirlin, *Phys. Rev. B* **74**, 235443 (2006).
- [61] S. Ryu and K. Nomura, *Phys. Rev. B* **85**, 155138 (2012).
- [62] In Ref. [18], $\mu_0\gamma_n e/v_F$ (v_F corresponds to c^* in our notation) is regarded as a scale factor for the relaxation rate to fit the experimental data. In the present paper, on the other hand, we do not regard $\mu_0\gamma_n e/c^*$ as the scale factor. We take $c^* = 10^4$ m/s as a typical value of the Fermi velocity.